ACS OMEGA

http://pubs.acs.org/journal/acsodf

Article

Impact of Controlled Storage Conditions on the Hydrolysis and Surface Morphology of Amorphous-UO_3

Alexa B. Hanson, Ian J. Schwerdt, Cody A. Nizinski, Rachel Nicholls Lee, Nicholas J. Mecham, Erik C. Abbott, Sean Heffernan, Adam Olsen, Michael R. Klosterman, Sean Martinson, Alexandria Brenkmann, and Luther W. McDonald, IV*

Cite This: *ACS Omega* 2021, 6, 8605−8615

Read Online

ACCESS | Metrics & More | Article Recommendations | Supporting Information

ABSTRACT: The hydration and morphological effects of amorphous (A)-UO_3 following storage under varying temperature and relative humidity have been investigated. This study provides valuable insight into U-oxide speciation following aging, the U-oxide quantitative morphological data set, and, overall, the characterization of nuclear material provenance. A-UO_3 was synthesized via the washed uranyl peroxide synthetic route and aged based on a 3-factor circumscribed central composite design of experiment. Target aging times include 2.57, 7.00, 14.0, 21.0, and 25.4 days, temperatures of 5.51, 15.0, 30.0, 45.0, and 54.5 °C, and relative humidities of 14.2, 30.0, 55.0, 80.0, and 95.8% were examined. Following aging, crystallographic changes were quantified via powder X-ray diffraction and an internal standard Rietveld refinement method was used to confirm the hydration of A-UO_3 to crystalline schoepite phases. The particle morphology from scanning electron microscopy images was quantified using both the Morphological Analysis of MAterials software and machine learning. Results from the machine learning were processed via agglomerative hierarchical clustering analysis to distinguish trends in morphological attributes from the aging study. Significantly hydrated samples were found to have a much larger, plate-like morphology in comparison to the unaged controls. Predictive modeling via a response surface methodology determined that while aging time, temperature, and relative humidity all have a quantifiable effect on A-UO_3 crystallographic and morphological changes, relative humidity has the most significant impact.

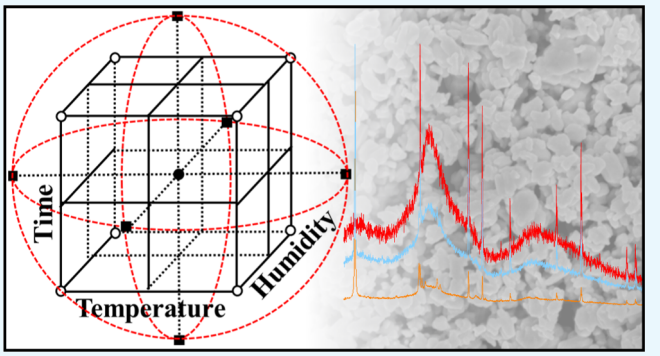

INTRODUCTION

The development of physiochemical U-oxide signatures is imperative in predicting the behavior and processing history of nuclear material. UO_3 is a key component of the nuclear fuel cycle and is produced on both the front and back ends in ore processing and refinement and spent fuel reprocessing, respectively.[1] Depending on the starting material, reaction conditions, and calcination temperature, UO_3 can form six different polymorphs: amorphous (A), α, β, γ, δ, and ε,[2−7] and is additionally known to undergo hydrolysis to several uranyl hydrates when exposed to liquid water, water vapor, and steam.[8]

The uranyl hydrates comprise the formula $[(UO_2)_xO_y-(OH)_z]^{(2x-2y-z)}$[9−12] and include three closely related species: schoepite, with generic formula $UO_3{\cdot}xH_2O$, where $2 < x \leq 2.5$; metaschoepite, $UO_3{\cdot}2H_2O$; and dehydrated schoepite, $UO_3{\cdot}xH_2O$ where $0.8 < x \leq 1$.[8,13] The speciation of the UO_3 system is largely complex and often represented by mixtures of polymorphs, amorphic material, and hydrolysis products.[14] The polymorphs and hydrolysis products of UO_3 have been widely characterized by powder X-ray diffraction (p-XRD) and have been recently studied by a variety of other analytical techniques including Raman and fluorescence spectroscopy,[1] differential thermal analysis,[6] thermogravimetric density functional theory,[13] optical and scanning electron microscopy (SEM),[15,16] microcalorimetry,[17] and extended X-ray absorption fine structure.[18]

The current literature recognizes additional studies must be completed to fully understand the degree of hydrolysis of UO_3 from three key hydrolysis factors: aging time, temperature, and relative humidity (RH).[1] Furthermore, it is acknowledged that, particularly in the case of p-XRD, where detecting amorphous material and minor crystalline components to less than 5% incorporation is limited, the implementation of additional

Received: January 24, 2021
Accepted: March 2, 2021
Published: March 16, 2021

https://dx.doi.org/10.1021/acsomega.1c00435
ACS Omega 2021, 6, 8605−8615

physiochemical signatures would be advantageous in determining the provenance of nuclear material.[15]

Previous work by Schwerdt et al. has statistically highlighted the importance of using multiple quantitative signatures for differentiation of material properties. For example, the authors distinguished between mixtures of A-UO_3 and α-UO_3 by using morphology as one quantifiable feature.[19] Morphology has been widely recognized as a signature for nuclear forensics as it is known to be influenced by a variety of synthetic processing parameters. Specifically, in recent years, research efforts have quantitatively proven the utility of U-oxide morphology in identifying starting and intermediate materials,[20,21] precipitation conditions,[22] thermal history,[22] oxidation rates,[23] mixtures of U-oxides,[24] and the presence of impurities.[25,26]

This work aims to expand the quantitative morphological data set for U-oxides by investigating the impact of controlled aging time, temperature, and RH on the hydrolysis and surface morphology of A-UO_3. Further understanding of temporal changes on the complexity of the $UO_3{\cdot}xH_2O$ system will additionally provide valuable insights into the storage history of U-oxides. While this research was highly focused in nuclear forensics, the knowledge of U-oxide oxidation plays an important role in the entire nuclear fuel cycle from ore processing to spent fuel reprocessing and to the long-term storage of spent nuclear fuel.[27,28] In addition, many recent studies have shown that there is an increased mobility of uranium from anaerobic sediments due to more extreme hydrologic and geochemical conditions which increases the flux of oxidants, nutrients, and biologic activity transported through them.[29,30] To fully understand the migration potential of uranium through these sediments, a fundamental understanding of its hydration and oxidation chemistry are needed.

In this study, A-UO_3 was synthesized via uranyl nitrate hexahydrate (UNH), $UO_2(NO_3)_2{\cdot}6H_2O$, by the washed uranyl peroxide synthetic route. UO_3 is regularly synthesized from UNH during spent fuel reprocessing, while the uranyl peroxide synthetic route is commonly utilized in the refinement and processing of U ore and is known for its environmental subsidies.[1,31] Washing by deionized water is commonly used in commercial practices to remove residual nitrates.[32] Following calcination to A-UO_3, samples were aged at varying time intervals in controlled temperature water baths, while simultaneously exposed to saturated aqueous salt solutions governing the RH. Storage conditions were based on a 3-factor circumscribed central composite design.

p-XRD was coupled with an internal standard Rietveld refinement method to quantify crystallographic changes due to the aging process. SEM with secondary electron detectors (SEM-SE) was utilized in conjunction with Morphological Analysis of MAterials (MAMA) software, Intellectus Statistics online software, and machine learning analysis via agglomerative hierarchical clustering analysis (HCA) for quantification of the morphology. A response surface model illustrating the effect of aging time, temperature, and RH on A-UO_3 will be presented.

EXPERIMENTAL SECTION

Design of Experiment. The design of experiment (DOE) was modeled using a three-factor circumscribed central composite design. The three process variables are represented by aging time, temperature, and RH. The central composite design combines a two-level embedded factorial design with two other parameters, center points and axial points. The center points represent the midrange values of the three variables, while the axial points set one variable to a high or low "axial" value, and the two other variables are set at the midrange value. The center points allow determination of any curvature within the system and the axial points allow estimation of the quadratic terms should any curvature occur. The factorial points are represented by low- and high-range values for each variable. In the circumscribed central composite design, the sample points designate a circle circumscribing the factorial square. Therefore, the three-factor response surface design designates a sphere circumscribing the factorial cube.[33−35] A graphical form of the DOE can be found in Supporting Information.

The DOE consists of 6 center points, 6 axial points, and 8 factorial points, where each point represents one sample. All points were replicated in triplicate for a total of 60 samples. An orthogonal blocking component was additionally utilized to reduce analysis time variance between samples. The DOE consists of three blocks containing 18, 18, and 24 samples, respectively. In each block, a control sample of unaged A-UO_3 was taken for analysis, representing 3 additional samples. Target aging times as calculated by the DOE included 2.57, 7.00, 14.0, 21.0, and 25.4 days, temperatures of 5.51, 15.0, 30.0, 45.0, and 54.5 °C, and relative humidities of 14.2, 30.0, 55.0, 80.0, and 95.8%. Significant figures for the target aging conditions are reported as a reflection of the experimental capability.

At the desired target temperatures, the RH could be controlled within approximately 1−4.5% of the targeted values based on ASTM's Standard Practice for Maintaining Constant RH by Means of Aqueous Solutions.[36] The observed values for each factor can be found in the Supporting Information. Responses were collected for each point and include quantitative MAMA data, percent mass increase from pre- to post-aged material, and crystalline versus amorphous composition as determined by Rietveld refinement.

Synthesis. Synthesis of A-UO_3 was based on previous work by Sweet et al.[15] and Cordfunke and Van Der Giessen.[32] Using the uranyl peroxide synthetic route, UNH, $UO_2(NO_3)_2{\cdot}6H_2O$, was dissolved in deionized water (18.2 MΩ) and a molar excess of 30% hydrogen peroxide, H_2O_2 to form the precipitate studtite, $(UO_2)O_2(H_2O)_2{\cdot}2H_2O$. The precipitate was washed with Millipore water to remove any residual nitrates and allowed to dry for 24 h at 80 °C to produce metastudtite, $(UO_2)(O_2)(H_2O)_2$. Samples were placed in 5 mL platinum crucibles seated within an aluminum oxide boat for calcination. The metastudtite was held at a calcination temperature of 400 °C for 8 h under 500 mL/min of purified air to yield A-UO_3. The well-washed uranyl peroxide guaranteed stability of the amorphous phase to at least 450 °C.[8]

To ensure consistency of the unaged A-UO_3 between samples, enough starting uranyl peroxide material for all 60 samples was prepared in the initial synthesis. Samples from blocks 2 and 3 were stored under vacuum (24 in Hg) as the more stable U-oxide, metastudtite, until they were needed for calcination to A-UO_3.

Aging Conditions. Following calcination to A-UO_3, the pre-aged weight was recorded for each sample and immediately placed under the respective storage conditions. The aging vessel setup was adapted from previous work by Reilly.[37] The aging vessels consist of an "outer" high density polyethylene (HDPE) vial containing 10 mL of saturated aqueous salt solution to control the RH of the vessel. The salt chosen for

https://dx.doi.org/10.1021/acsomega.1c00435
ACS Omega 2021, 6, 8605−8615

each sample type was dependent upon the storage temperature and desired humidity.[36]

An "inner" HDPE vial containing the unaged A-UO_3 was seated inside the outer vial and left open to its atmosphere controlled by the saturated aqueous salt solution. The outer vial was sealed by the HDPE cap and subsequently submerged in controlled temperature water baths for aging. By completely submerging the aging vessels, the formation of condensation on the vessel walls could be mitigated. Magnets were attached by waterproof sealant to the bottom of the vessels and secured on metallic plates within the water baths. When the desired aging times were reached, the vessels were removed from the water baths and thoroughly dried before opening as to not allow any moisture to fall into the sample. The color of the sample was recorded to note any qualitative change in the material, and the presence of undissolved salt remaining in the outer vessel was documented to verify the desired RH was held for the full aging time. Figures further representing the aging vessel setup can be found in the Supporting Information.

Each of the 15 sample types, point types, and corresponding salt types are shown in Table 1. For organizational purposes, 7 samples: the control, two center, two factorial, and two axial points were chosen as crystallographically and morphologically representative samples for the discussion of this study. These samples are abbreviated in figures as letters A−G and are included in Table 1 for reference. Raw and analyzed data for all samples can be found in the Supporting Information.

Table 1. Each of the 15 Sample Types Including 6 Center, 6 Axial, and 8 Factorial Points[a]

aging time (d)	temperature (°C)	relative humidity (%)	salt	point type	letter abb.
2.57	30.0	55.0	sodium bromide	axial	
7.00	15.0	30.0	magnesium chloride	factorial	
7.00	15.0	80.0	sodium chloride	factorial	
7.00	45.0	30.0	magnesium chloride	factorial	
7.00	45.0	80.0	potassium chloride	factorial	
14.0	5.51	55.0	sodium bromide	axial	
14.0	30.0	95.8	potassium sulfate	axial	
14.0	30.0	14.2	lithium chloride	axial	G
14.0	30.0	55.0	sodium bromide	center	B & C
14.0	54.5	55.0	sodium bromide	axial	F
21.0	15.0	30.0	magnesium chloride	factorial	
21.0	15.0	80.0	sodium chloride	factorial	
21.0	45.0	30.0	magnesium chloride	factorial	E
21.0	45.0	80.0	potassium chloride	factorial	D
25.4	30.0	55.0	sodium bromide	axial	

[a]Only one center point sample is listed as the storage conditions were the same for each point. The RH for each sample was controlled by aqueous salt solutions, and the corresponding salt used for each sample type is shown below. Sample letter "A" denotes the control and is not included.

Powder X-ray Diffraction. Following aging, the post-aged weight was recorded for each sample and immediately prepared for p-XRD analysis. Prior to p-XRD analysis, all samples were ground in a high-purity aluminum oxide mortar and pestle using 2 mL *n*-pentane. Samples were then sieved to less than 20 μm with an ASTM E11 certified no. 635 test sieve to ensure consistency in the crystallite size across samples. For the internal standard method with Rietveld refinement, sieved samples were spiked with 20% (by weight) NIST SRM 674b Cr_2O_3, and thoroughly mixed in a 5 mL dram vial on a vortex mixer. Samples were loaded on a P-type, B-doped silicon crystal zero diffraction plate and characterized using a Bruker D2 Phaser. Each scan was performed for 107 min at a range of 10−70° 2θ, 0.02° step size, and 2 s per step. Samples were rotated at 15 rpm to account for any preferential orientation of the crystals. A 0.6 mm divergence slit size, 1 mm antiscattering beam knife height, and 3 mm receiving slit size were used for the characterizations. Refined parameters include specimen displacement, unit cell parameters *a*, *b*, and *c* [Å], profile parameters U, V, and W, peak shapes 1 and 2, and thermal displacement parameter, β. All samples were refined by the order of parameters listed.

Scanning Electron Microscopy. SEM analysis was performed within 12 h of aging completion. Samples were prepared for SEM prior to being ground, sieved, and spiked for the internal standard method. Each sample (5−10 mg) was dusted onto a 12.7 mm aluminum pin stub mount with an adhesive 12 mm conductive carbon tab and lightly tapped to remove any loose material. The stubs were coated with a 200 ± 1 Å Au/Pd film to prevent excessive surface charging. Image acquisition was completed on a FEI Nova NanoSEM 630 high-resolution SEM using the through the lens SE detector at an accelerating voltage of 5 kV. As particle sizes varied depending on sample hydrolysis, acquired image magnifications ranged from 10,000 to 100,000*x*.

Quantitative Morphological Analysis. Manual quantitative analysis on the SEM imagery was completed using MAMA version 2.1 software developed by Los Alamos National Laboratory.[38] The software algorithm and particle segmentation procedure has been described previously by Olsen et al.[39] Multiple users were utilized in completing the manual segmentation to help eliminate the potential for single user bias. The obtained data was statistically analyzed via JMP Pro version 15.0.0[40] and Intellectus Statistics online software[41] and modeled via the response surface model in JMP. Over 15,000 particles were manually segmented for analysis.

To further elucidate any observable trends from the MAMA data, machine learning analysis via agglomerative HCA was employed in conjunction with the manual quantitative analysis. HCA is a multivariate technique that successively joins similar clusters of data until all sets have been merged together.[42,43] MAMA segmentation data from aged A-UO_3 particles was preprocessed by principal component analysis (PCA) to reduce the dimensionality of the data set, then standardized by mean-centering and scaling. HCA with the Ward's (minimum variance) linkage method was iterated until some distance threshold was reached.[44] PCA, data preprocessing, and clustering were performed with the scikit-learn machine learning library for Python.

https://dx.doi.org/10.1021/acsomega.1c00435
ACS Omega 2021, 6, 8605−8615

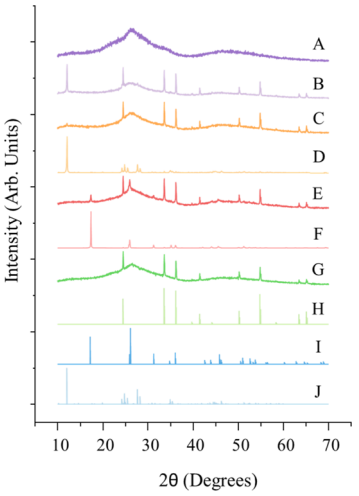

Figure 1. Comparison of p-XRD diffraction spectra of samples aged at varying times, temperatures, and relative humidities. (A) Unaged A-UO_3; (B,C) center points aged at 14.0 d, 30.0 °C, 55.0% RH; (D) factorial point aged at 21.0 d, 45.0 °C, 80.0% RH; (E) factorial point aged at 21.0 d, 45.0 °C, 30.0% RH; (F) axial point aged at 14.0 d, 54.5 °C, 55.0% RH; (G) axial point aged at 14.0 d, 30.0 °C, 14.2% RH; (H) Cr_2O_3 reference pattern. ICSD #90158; and (I) dehydrated schoepite, α-$UO_2(OH)_2$, reference pattern. ICSD #9116 (J) metaschoepite, $UO_3{\cdot}2H_2O$, reference pattern. ICSD #76895.

RESULTS AND DISCUSSION

Powder X-ray Diffraction. The amorphic and crystalline compositions of each sample were established by p-XRD analysis. The characterization and subsequent Rietveld refinement were completed using Malvern Panalytical's X'Pert Highscore Plus version 4.9 software.[45] Figure 1 illustrates the normalized intensity spectra representative of the unaged sample and two factorial, axial, and center point samples designated as A−G, as listed in Table 1. Reference patterns were obtained from the NIST Inorganic Crystal Structure Database (ICSD). The spectra are compared against reference peak locations for Cr_2O_3 (ICSD #90158), dehydrated schoepite (approximately isostructural with α-$UO_2(OH)_2$,[46] ICSD #9116), and metaschoepite (ICSD #76895).

Figure 1A is representative of the unaged A-UO_3 control samples. 1B and 1C are center point patterns aged at 14.0 d, 30.0 °C, and 55.0% RH. 1B illustrates a qualitatively larger presence of metaschoepite than 1C, with the most significant $UO_3{\cdot}2H_2O$ peak occurring at 12.1° (2θ). Of the 18 total center point samples, a wide distribution of metaschoepite abundance was qualitatively observed from the p-XRD spectra. The large distribution between replicates suggests the center point aging conditions may be an inflection point for the formation of schoepite phases, and the formation of these phases may occur rapidly once the aging process begins. This is discussed further in the following sections.

Two factorial points are represented by 1D and 1E. Samples aged at 21.0 d, 45.0 °C, and 80.0% RH (1D) indicate the presence of metaschoepite, while samples aged at 21.0 d, 45.0 °C, and 30.0% RH (1E) were largely amorphous. However, 1E shows the presence of dehydrated schoepite, with the most significant α-$UO_2(OH)_2$ peaks occurring at 17.2 and 26.1° (2θ). 1F and 1G are representative of two axial points aged at 14.0 d, 54.5 °C, and 55.0% RH, and 14.0 d, 30.0 °C, and 14.2% RH, respectively. 1F is observed to be largely dehydrated schoepite, while 1G appears amorphous. In contrast to center points 1B and 1C, the material aged under the conditions of 1D, 1E, 1F, and 1G were consistent across replicates (as is true for all other axial and factorial point replicates, found in the Supporting Information), further suggesting the center point aging conditions of 14.0 d, 30.0 °C, and 55.0% RH serve as a possible inflection point for the formation of schoepite phases. Spectra comparisons for center point replicates and all other samples can be found in the Supporting Information.

Rietveld Refinement of Aged p-XRD Patterns. Rietveld refinement via the internal standard method was utilized for quantification of the observed qualitative changes in the p-XRD spectra. In the internal standard method, samples are spiked with a known amount of 100% crystalline standard material (in this case 20 wt % NIST SRM 674b Cr_2O_3) and normalized for quantitative phase analysis. The internal standard method is highly useful for quantification of amorphous material in the sample; amorphous phases are not directly detected by XRD and, if present, amorphous material will result in the quantitative overestimation of

Table 2. Comparison of Rietveld Refinement Results for All Samples Using the Internal Standard Method[a]

aging conditions	metaschoepite ($UO_3{\cdot}2H_2O$) (%)	dehydrated schoepite ($UO_2(OH)_2$) (%)	amorphous UO_3 (%)	letter abb.
2.57 d, 30.0 °C, 55.0%	0.1 ± 0.1	0.2 ± 0.2	99.7 ± 0.4	
7.00 d, 15.0 °C, 55.0%	0.6 ± 0.4	0.4 ± 0.3	99.27 ± 0.05	
7.00 d, 15.0 °C, 80.0%	31 ± 3	0.07 ± 0.09	69 ± 3	
7.00 d, 45.0 °C, 30.0%	0.2 ± 0.1	1 ± 1	98 ± 1	
7.00 d, 45.0 °C, 80.0%	53 ± 2	0.05 ± 0.05	47 ± 2	
14.0 d, 5.51 °C, 55.0%	0.2 ± 0.1	0.4 ± 0.5	99.4 ± 0.6	
14.0 d, 30.0 °C, 95.8%	71.9 ± 0.6	0.7 ± 0.5	27 ± 1	
14.0 d, 30.0 °C, 14.2%	0.13 ± 0.05	0.1 ± 0.1	99.7 ± 0.1	G
14.0 d, 30.0 °C, 55.0%	6 ± 6	0.4 ± 0.7	93 ± 6	B & C
14.0 d, 54.5 °C, 55.0%	0.3 ± 0.3	96 ± 2	4 ± 2	F
21.0d, 15.0 °C, 30.0%	0.2 ± 0.1	0.2 ± 0.2	99.7 ± 0.3	
21.0 d, 15.0 °C, 80.0%	62 ± 6	0.03 ± 0.05	38 ± 4	
21.0 d, 45.0 °C, 30.0%	0.2 ± 0.1	2.7 ± 0.7	96 ± 2	E
21.0 d, 45.0 °C, 80.0%	76 ± 3	0.03 ± 0.05	24 ± 3	D
25.4 d, 30.0 °C, 55.0%	23 ± 3	0.03 ± 0.05	76 ± 3	

[a]Results are shown as an average for each sample ± the error, 1σ. Samples with high humidity represent hydration to metaschoepite, $UO_3{\cdot}2H_2O$, while samples with high temperatures and lower humidity represent the shift to dehydrated schoepite, $UO_2(OH)_2$.

https://dx.doi.org/10.1021/acsomega.1c00435
ACS Omega 2021, 6, 8605−8615

crystalline phases in the sample. However, if a known amount of crystalline standard material is added prior to analysis, a correction factor from the overestimation of crystalline phases can be calculated. The correction factor is then used to calculate the weight percentage of the otherwise undetected amorphous material[45,47,48]

$$\text{amorphous wt \%} = 100 - \sum_{i=1}^{n} \text{calculated wt \%}_i \times \frac{\text{standard wt \%}}{\text{calculated wt \%}_{\text{standard material}}}$$

In addition to sample phase concentrations, the weighted-profile R value, R_{wp}, statistically expected R value, R_{exp}, and goodness of fit (GOF) were calculated for each refinement. R_{wp} compares the calculated versus observed data, while R_{exp} corresponds to the quality of the data. The GOF is represented by the ratio of R_{wp} to R_{exp} squared and should approach 1 in quality refinements. In the case of highly amorphous samples, GOF may be less than one.[49] R_{wp}, R_{exp}, and GOF for all sample refinements can be found in Supporting Information.

Comprehensive Rietveld refinement results are shown in Table 2, while representative samples B-G are illustrated in Figure 2. As each center, axial, and factorial points were

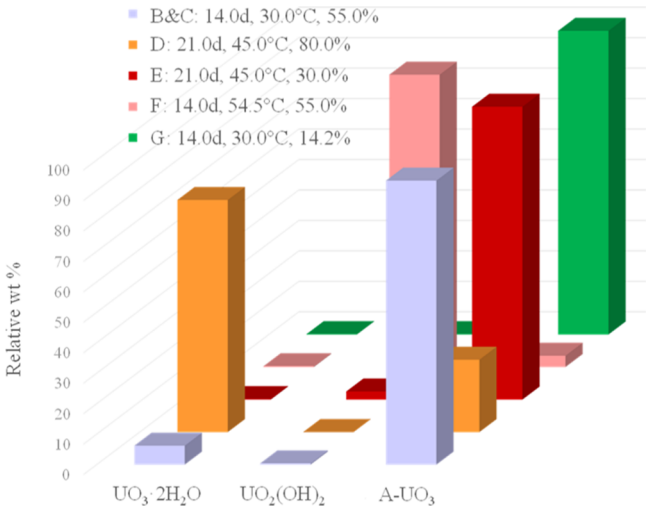

Figure 2. Graphical comparison of Rietveld refinement results using the internal standard method. (B,C) Center points aged at 14.0 d, 30.0 °C, 55.0% RH; (D) factorial point aged at 21.0 d, 45.0 °C, 80.0% RH; (E) factorial point aged at 21.0 d, 45.0 °C, 30.0% RH; (F) axial point aged at 14.0 d, 54.5 °C, 55.0% RH; (G) axial point aged at 14.0 d, 30.0 °C, 14.2% RH. Samples with high humidity represent hydration to metaschoepite, $UO_3{\cdot}2H_2O$, while samples with high temperatures and lower humidity represent hydration to dehydrated schoepite, $UO_2(OH)_2$.

replicated in triplicate, results are reported as averages with the error reported as $\pm 1\sigma$. In correspondence with the qualitative p-XRD results, the center point samples 2B and C aged at 14.0 d, 30.0 °C, and 55.0% RH exhibited a wide range of crystalline phase concentrations as shown by the large error in quantified metaschoepite (6 ± 6%) and A-UO_3 (93 ± 6%) phases. Likewise, factorial point 2D was found to be primarily metaschoepite (76 ± 3%), while 2E was largely A-UO_3 (96 ± 2%) but contained a small percentage of dehydrated schoepite (2.7 ± 0.7%). Axial points 2F and 2G were additionally consistent with the qualitative p-XRD results, with 2F having nearly entirely converted to dehydrated schoepite (96 ± 2%), and 2G highly amorphous (99.7 ± 0.1%). The lesser error in samples 2D−G further supports the notion of center point samples 14.0 d, 30.0 °C, and 55.0% RH, representing a hydrolysis inflection point in the aging conditions.

Overall, longer aging times coupled with higher temperatures and relative humidities corresponded to the conversion of A-UO_3 to crystalline schoepite phases, the refinement results suggest that each of the three factors have an effect on the rate of conversion. For example, samples aged at 2.57, 14.0, and 25.4 d at 30.0 °C and 55.0% RH exhibited a steady increase in the metaschoepite concentration (0.1 ± 0.1 to 23 ± 3%). However, aging conditions 7.00 and 21.0 d at 15.0 °C, 30.0% RH were both mainly A-UO_3 and could not be quantifiably distinguished despite a two-week difference in aging time. Notably, samples with the same aging times at higher temperatures and RH could be quantifiably differentiated. For instance, samples aged at 7.00 d, 45.0 °C, and 80.0% RH had a metaschoepite concentration of 53 ± 2%, while samples aged at 21.0 d, 45.0 °C, and 80.0% RH were 76 ± 3% metaschoepite. These results suggest aging time has a less quantifiable effect at lower temperatures and relative humidities but has a greater effect at high temperatures and relative humidities.

Likewise, samples with higher temperatures had an increasing effect on crystalline composition; samples aged at 14.0 d, 5.51 °C, and 55.0% RH were primarily A-UO_3 (99.4 ± 0.6%), while center point samples 14.0 d, 30.0 °C, and 55.0% RH contained a wide range in quantifiable metaschoepite (6 ± 6%). As previously mentioned, samples aged at 14.0 d, 54.5 °C, and 55.0% RH were nearly entirely dehydrated schoepite (96 ± 2%). Similar temperature effects were observed in samples 7.00 d, 15.0 °C, 30.0% RH and 7.00 d, 45.0 °C, 30.0% RH; 7.00 d, 15.0 °C, 80.0% RH and 7.00 d, 45.0 °C, 80.0% RH; 21.0 d, 15.0 °C, 80.0% RH and 21.0 d, 45.0 °C, 80.0% RH (conversion to metaschoepite); and 21.0 d, 15.0 °C, 30.0% RH, and 21.0 d, 45.0 °C, 30.0% RH (conversion to dehydrated schoepite). The increases in metaschoepite or dehydrated schoepite concentration in each case suggests temperature plays a definitive role in the hydrolysis of A-UO_3 to crystalline schoepite phases.

Similarly, when comparing relative humidities, samples aged at 7.00 d, 45.0 °C, and 30.0% RH were primarily A-UO_3, while samples aged at 7.00 d, 45.0 °C, and 80.0% RH had a large increase in the metaschoepite composition (53 ± 2%). A similar effect of humidity with conversion to metaschoepite was observed in samples 7.00 d, 15.0 °C, 30.0% RH and 7.00 d, 15.0 °C, 80.0% RH; 14.0 d, 30.0 °C, 14.2% RH and 14.0, 30.0 °C, 55.0% RH and 14.0 d, 30.0 °C, 95.8%; 21.0 d, 15.0 °C, 30.0% RH and 21.0 d, 15.0 °C, 80.0% RH; and 21.0 d, 45.0 °C, 30.0% RH and 21.0 d, 45.0 °C, 80.0% RH, suggesting humidity additionally has a large effect on the hydrolysis of A-UO_3.

Dehydrated schoepite formed at temperatures 45.0 and 54.5 °C when relative humidities were 30.0 and 55.0%, respectively. Samples with relative humidities greater than 55.0% formed metaschoepite, regardless of temperature. Thus, overall, the refinement results illustrate the formation of dehydrated schoepite at high temperatures and mid-range relative humidities, and the formation of metaschoepite at high humidities. All samples with high-humidity aging conditions (>55.0%), plus samples aged at 14.0 d, 54.5 °C, 55.0% RH and

https://dx.doi.org/10.1021/acsomega.1c00435
ACS Omega 2021, 6, 8605−8615

25.4 d, 30.0 °C, 55.0% RH, were discernible from each other via Rietveld refinement.

Notably, Sweet et al. observed the formation of dehydrated schoepite from α and γ-UO_3 after aging in a capped vial at room temperature and 20−30% RH for 34 and 45 days, respectively. Post-aged Rietveld refinement indicated the γ-UO_3 had hydrolyzed to 25% dehydrated schoepite, while the longer-aged α-UO_3 was 90% dehydrated schoepite and 5% metaschoepite.[15] The formation of dehydrated schoepite at room temperature in Sweet's work combined with the findings in this study (A-UO_3 hydrating to 96 ± 2% dehydrated schoepite after 14.0 days at 54.5 °C, and 55.0% RH) further suggests temperature is a component to the hydration of UO_3 to dehydrated schoepite. Furthermore, the formation of 5% metaschoepite in the α-UO_3 sample implies admixtures of dehydrated schoepite and metaschoepite will occur around room temperature and RH conditions, but the conversion to metaschoepite occurs at a slower rate.

In other work by Wilkerson et al., α-UO_3 was aged for 5 days *in situ* in a Bruker D8 Advance Diffractometer at 60 °C and 70% RH. Results from the XRD patterns indicated no apparent phase changes.[50] Interestingly, in the current study, over 50% metaschoepite formation was observed after aging for 7.00 days at a lesser temperature, 45.0 °C, and greater RH, 80.0%, albeit with a different UO_3 polymorph in question, A-UO_3. This agrees with work by Rodgers and Dyck,[51] and an Incident Analysis Report by Golder Associates Inc.,[52] which found that UO_3 synthesized at higher temperatures, that is, crystalline UO_3 polymorphs, are less reactive in water than the amorphous phase. Nonetheless, the results from the current study suggest the hydration of A-UO_3 can initialize rapidly under the right conditions, and high RH may have a significant effect. Future studies comparing hydrolysis between UO_3 polymorphs would be a substantial development to the understanding of the $UO_3{\cdot}xH_2O$ system.

Scanning Electron Microscopy. To further characterize each aging condition and expand the U-oxide morphological data set, powders of each aged sample were analyzed using SEM. Over 1,000 SEM images were collected for image analysis. Figure 3 depicts changes in particle morphology between samples due to hydrolysis. Each image was qualitatively analyzed using a lexicon developed by Tamasi et al. for consistent description of the nuclear material morphology.[53] Figure 3A shows the unaged A-UO_3 morphology comprised of a clumped/massive conglomerate of irregular/clumped, sub-rounded sub-particles composed of semirounded grains. It consists of somewhat-rough surface features. 3B and 3C are center point samples aged at 14.0 d, 30.0 °C, and 55.0% RH. Both samples appear more uniform in morphologic distribution than 3A, and, despite 3B containing more metaschoepite than 3C as indicated by the p-XRD analysis and Rietveld refinement, the samples appear to be qualitatively similar to each other. The morphology can be described as a clumped/massive agglomerate of sub-rounded sub-particles composed of semirounded grains. It consists of somewhat-smooth surface features, and the sub-particles are more reticulated when compared to 3A.

Factorial points 3D and 3E were aged at 80.0 and 30.0% RH, respectively, but were held at the same aging times and temperatures, 21.0 d and 45.0 °C. 3E is comparable to the same descriptors for 3B and C and cannot be qualitatively distinguished via SEM despite the presence of dehydrated schoepite from the p-XRD analysis. However, 3D was shown

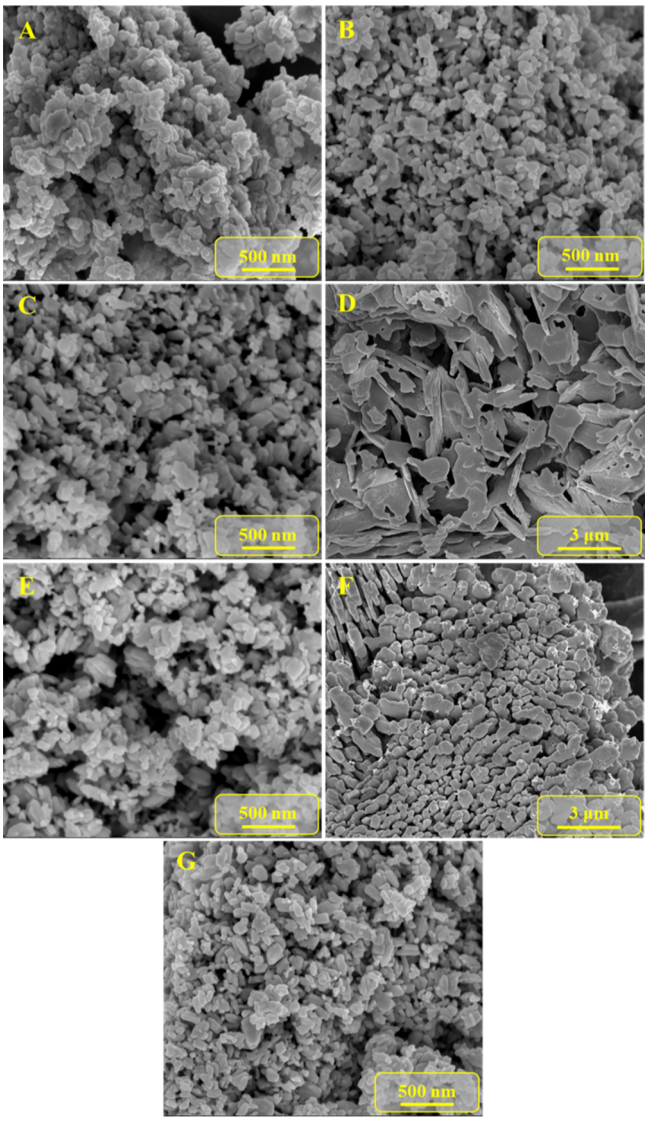

Figure 3. Comparison of SEM imagery of samples aged at varying times, temperatures, and relative humidities. (A) Unaged A-UO_3; (B,C) Center point aged at 14.0 d, 30.0 °C, 55.0% RH; (D) Factorial point aged at 21.0 d, 45.0 °C, 80.0% RH; (E) factorial point aged at 21.0 d, 45.0 °C, 30.0% RH; (F) axial point aged at 14.0 d, 54.5 °C, 55.0% RH; and (G) axial point aged at 14.0 d, 30.0 °C, 14.2% RH.

to have a large composition of metaschoepite from p-XRD and exhibits a drastically different, larger particle morphology. 3D is a clumped/massive conglomerate of scaled/layered/lamellae, that is, plate-like crystals, with thick tabular grains. The surface morphology is somewhat smooth, and some of the plate-like features contain holes.

Axial points 3F and G were aged at 14.0 d, 54.5 °C, and 55.0% RH, and 14.0 d, 30.0 °C, and 14.2% RH, respectively. 3F was determined to have a large abundance of dehydrated schoepite from p-XRD analysis and Rietveld refinement and correspondingly has a greatly different morphology. Qualitatively, 3F is a clumped/massive conglomerate of sub-rounded sub-particles comprised of both semirounded and blocky/stubby grains. The spatial arrangement of sub-particles was observed to be both clumped/irregular and parallel in nature. 3G appears largely amorphous in composition from the p-XRD analysis and can be categorized under the same descriptors as 3B, C, and E. Additional SEM imagery for

https://dx.doi.org/10.1021/acsomega.1c00435
ACS Omega 2021, 6, 8605−8615

samples 3A−G and all other samples can be found in Supporting Information.

While samples 3B, C, E, and G appeared more uniform in composition than the control, they were not readily distinguishable from one another via qualitative image analysis. This is in agreement with the Rietveld refinement results, which showed statistically similar A-UO_3 concentrations for 3B, C, E, and G; conclusively, highly amorphous samples could also not be distinguished from one another via qualitative SEM analysis. Notably, samples aged under high humidity conditions (>55.0%) additionally could not be qualitatively discerned from one other, despite their metaschoepite concentrations being quantifiably different via Rietveld refinement.

Nonetheless, the extremely differing particle morphology of 3D and 3F coupled with the p-XRD and Rietveld refinement analysis further suggests U-oxide storage conditions play a great role in sample composition and morphology. These results are in agreement with previous U-oxide aging studies, which found overall longer aging time, higher temperature, and RH correspond to greater sample hydrolysis[18,50] and larger particle morphology.[16,37] Other works have shown that increases in uranyl acetate concentration cause faster crystal growth kinetics in uranium oxide hydroxide hydrate.[54] It is possible that water represents a similar morphological component in the case of UO_3 hydrolysis, but overall, the mechanisms behind the observed morphological changes are presently unknown.

Quantitative Morphological Analysis. While highly amorphous samples are readily distinguishable from samples containing primarily metaschoepite or dehydrated schoepite using XRD spectra, they are not qualitatively discernible from each other based on their morphology. To further elucidate morphological change due to aging conditions, quantitative analysis was pursued in an effort to establish additional statistical difference between samples. Two techniques were used, MAMA segmentation analysis via JMP and Intellectus Statistics, and machine learning via agglomerative HCA.

Using the MAMA software, over 15,000 particles were manually segmented for quantitative analysis. Each discrete particle was classified according to 14 different attributes such as pixel area, perimeter and area convexity, circularity, and ellipse aspect ratio. All attributes are described in detail elsewhere by Gaschen et al.[55] MAMA data was collated and processed using Intellectus Statistics and JMP software. It was determined via analysis in JMP that the data followed a non-normal distribution. All data was transformed by natural logarithm to omit this issue for statistical analysis.

Due to the large morphological difference between largely amorphous (aging conditions with ≤55.0% RH, referred to here as "nonhydrolyzed") and primarily hydrated material (aging conditions with >55.0% RH, referred to here as "hydrolyzed"), the data set additionally had unequal variance. Furthermore, as the hydrolyzed material is comprised of much larger particles, there were not as many particles available for manual segmentation and the data set thus consists of unequal sample sizes. Unequal variance and unequal sample sizes pose a challenge to statistical tests such as analysis of variance (ANOVA) or Tukey Kramer, which assume homogeneity of variance for accurate analysis. However, the Kruskall−Wallis test serves as a nonparametric alternative one-way ANOVA and does not assume normality.[56]

Therefore, to prove statistical difference between non-hydrolyzed and hydrolyzed material, Kruskall−Wallis rank sum tests were performed using Intellectus Statistics.[41] Attributes utilized for analysis included pixel area, convex hull area, ellipse aspect ratio, circularity, perimeter convexity, area convexity, equivalent circle diameter, vector area, and diameter aspect ratio. All attributes chosen for analysis were based on the verification for correct implementation and accurate calculations defined by Porter and Ruggiero.[57]

The Kruskall−Wallis results were significant with all attributes being listed at a 95% confidence interval, indicating the mean rank for each attribute was discernible between samples. Post-hoc pairwise comparisons between all aging conditions illustrated nonhydrolyzed samples were quantifiably differentiable from hydrolyzed samples, which agrees with the qualitative morphological analysis. With the statistical difference established, nonhydrolyzed samples and hydrolyzed samples were treated as two separate data sets. It should be noted that samples under aging conditions 25.4 d, 30.0 °C, 55.0% RH and 14.0 d, 54.5 °C, 55.0% RH were included in the hydrolyzed data set as they exhibited a larger particle morphology than the nonhydrolyzed samples and were found to contain metaschoepite and dehydrated schoepite from MAMA analysis and Rietveld refinement, respectively. Control samples were included in the nonhydrolyzed data set as they were found to be discernible from the hydrolyzed samples by the Kruskall−Wallis test.

Both data sets were transformed and tested for normal distribution and equal variance. Each data set was also randomized to ensure equal sample sizes for each aging condition, where the largest possible number of particles was chosen based on the aging condition with the least number of segmented particles. This amounted to 810 particles per aging condition for nonhydrolyzed samples and 135 particles per aging condition for hydrolyzed samples. The Tukey−Kramer honest significant difference test was then performed for both data sets.

Results for the hydrolyzed samples showed aging conditions 14.0 d, 54.5 °C, 55.0% RH (96 ± 2% dehydrated schoepite), 14.0d, 30.0 °C, 95.8% RH (71.9 ± 0.6% metaschoepite), and 25.4 d, 30.0 °C, 55.0% RH (23 ± 3% metaschoepite) were quantifiably distinguishable from all other samples by vector area at a 95% confidence interval. Several other particle attributes can additionally be used to distinguish conditions 14.0 d, 54.5 °C, 55.0% RH and 14.0 d, 30.0 °C, 95.8% RH. All other hydrolyzed samples were not individually discernible by quantification of the morphology despite being quantifiably differentiable by Rietveld refinement.

Nonhydrolyzed sample 14.0 d, 30.0 °C, 14.2% RH (99.7 ± 0.1 A-UO_3) can be distinguished from all other samples by diameter aspect ratio, while aging condition 21.0 d, 15.0 °C, 30.0% (99.7 ± 0.3 A-UO_3) can be discerned by area convexity. It is unknown why these aging conditions may be quantifiably discernible. Connecting letters report illustrating the Tukey−Kramer results for the vector area of the hydrolyzed data set and diameter aspect ratio and area convexity for the nonhydrolyzed data set can be found in Supporting Information. Table S-3, in Supporting Information additionally, provides a breakdown of all significantly quantifiable attributes for each aging condition, if applicable.

To further elucidate any trends from the MAMA data, machine learning agglomerative HCA was explored. One hundred particles were randomly sampled for each of the 15

https://dx.doi.org/10.1021/acsomega.1c00435
ACS Omega 2021, 6, 8605−8615

aging parameter sets prior to clustering analysis to remove any effects of imbalanced data sets. PCA of the MAMA data determined reducing the data's dimensionality to 4 PCs was sufficient to explain over 95% of the data set's variance. Each of the PCA weights can be seen by heatmap in the Supporting Information.

HCA with a Euclidean distance threshold of 12.0 resulted in 2 distinct clusters. For each time, temperature, and RH aging parameter, the fraction of particles belonging to either cluster (0 or 1) was used to identify how each parameter affects particle morphology. Figure 4 shows the fractions for each

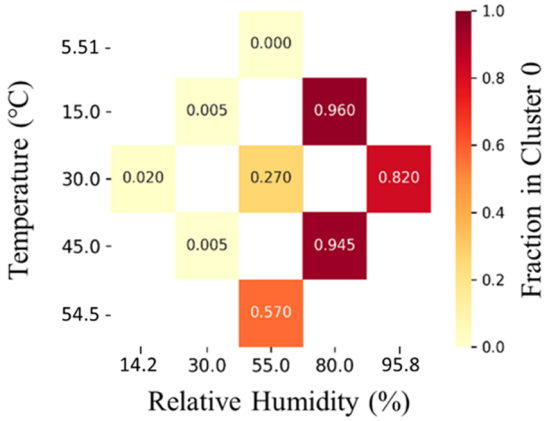

Figure 4. HCA heat map of Cluster 0 fractions for each aging temperature and RH combination. As the RH increases, the fraction of particles in Cluster 0 increases. Supporting Information Figures S-85 and S-86 show a similar trend in which longer aging times and highly RH corresponds to more particles in Cluster 0. These results prove that morphological changes are more dependent on aging time and RH than temperature, corroborating the earlier XRD results which found similar conclusions.

aging temperature and RH parameter, where the fraction of particles belonging to cluster 0 increases as RH increases. Nonetheless, at 55.0% RH, the fraction of particles assigned to cluster 0 increase as the aging temperature increases from 5.51 to 54.5 °C, which reflects the increasing particle morphology of the dehydrated schoepite sample aged at 14.0 d, 54.5 °C, and 55.0% RH. Supporting Information Figures S-85 and S-86 show a similar trend, in which longer aging times and higher RH lead to more particles in cluster 0. The HCA results suggest aging time and RH have the most significant quantifiable effect in changes to A-UO_3 particle morphology. This is corroborated by, yet expands on the Rietveld refinement results, which illustrated each of the three factors had a quantifiable effect on the hydration of A-UO_3.

Response Surface Methodology Model. The response data from MAMA segmentation, % increase in mass for each sample, and crystalline and amorphous content obtained from Rietveld refinement were inputted into the three-factor circumscribed central composite DOE. Averaged, untransformed values were used for each MAMA attribute. The independent variable aging time was modified to reflect the observed aging time. Likewise, the RH independent variable was modified to reflect the values defined by ASTM's Standard Practice for Maintaining Constant RH by Means of Aqueous Solutions.[36] The Supporting Information includes the aging times and relative humidities modeled by the DOE versus the observed values.

Table 3 shows the overall variable importance for aging time, temperature, and RH. The summary accounts for all responses

Table 3. Overall Variable Importance of Aging Time, Temperature, and RH to the Response Surface Model[a]

Variable	Main Effect	Total Effect
Relative Humidity (%)	0.666	0.716
Aging Time (d)	0.151	0.186
Temperature (°C)	0.102	0.131

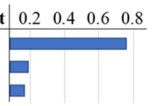

[a]RH had the greatest quantifiable impact, followed by aging time and temperature.

inputted into the surface model and is calculated by Monte Carlo samples drawn from the minimum and maximum observed values for each response. The main effect is the importance index that reflects the contribution of each factor alone, not in combination with other factors, while the total effect reflects both the factor alone and in combination with other factors. The results indicate RH had the overall greatest quantifiable effect, followed by aging time and temperature. A full breakdown of prediction profilers for each response can be found in the Supporting Information. Notably, temperature had the greatest quantifiable impact for the % dehydrated schoepite response in agreement with the Rietveld refinement results. All other responses largely followed the overall variable importance trend, with RH being the greatest factor. One exception is pixel area, in which RH and aging time were found to have an equal effect.

An illustrated example for % metaschoepite (corresponding to the hydroylsis of A-UO_3) is shown in Figures 5−7. Figure 5 depicts % metaschoepite modeled as a function of aging time and RH. As aging time increases from 0 to 30 days and RH increases from 0 to 100%, % metaschoepite has a direct correlation and drastically increases. In agreement with Rietveld refinement and agglomerative HCA, aging time, and RH both have a quantifiable effect on the hydrolysis of A-UO_3,

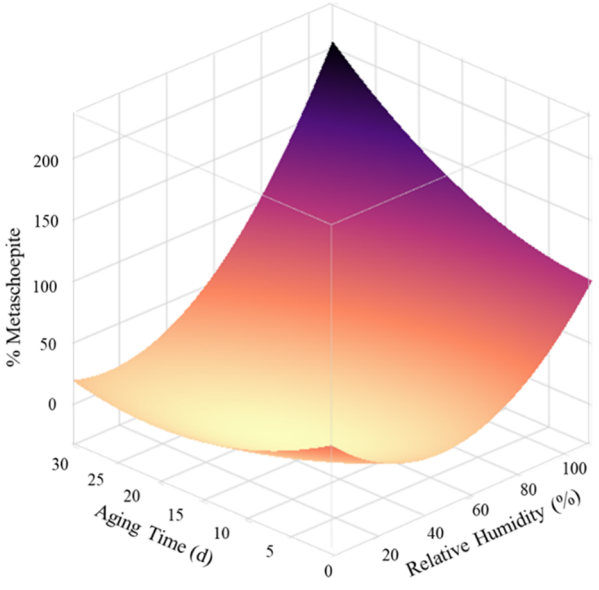

Figure 5. Response surface plot illustrating the effect of aging time and RH on the increase of metaschoepite from the hydration of A-UO_3. The response was held at the center point aging conditions of 14.0 d, 30.0 °C, and 55.0% RH.

https://dx.doi.org/10.1021/acsomega.1c00435
ACS Omega 2021, 6, 8605−8615

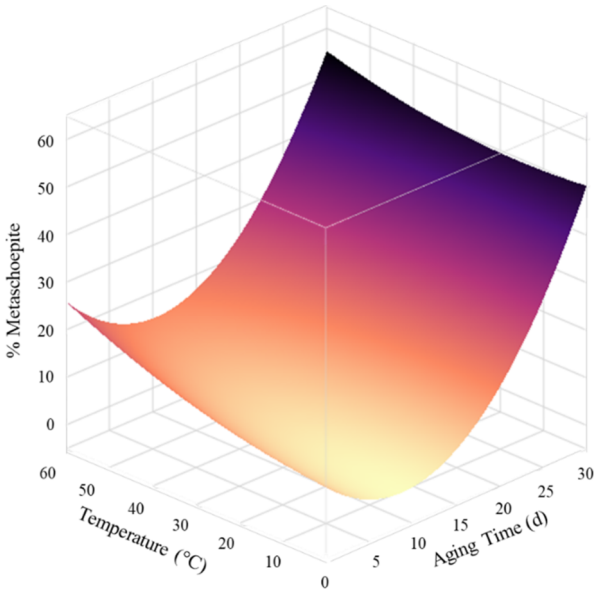

Figure 6. Response surface plot illustrating the effect of aging time and temperature on the increase of metaschoepite from the hydration of A-UO_3. The response was held at the center point aging conditions of 14.0 d, 30.0 °C, and 55.0% RH.

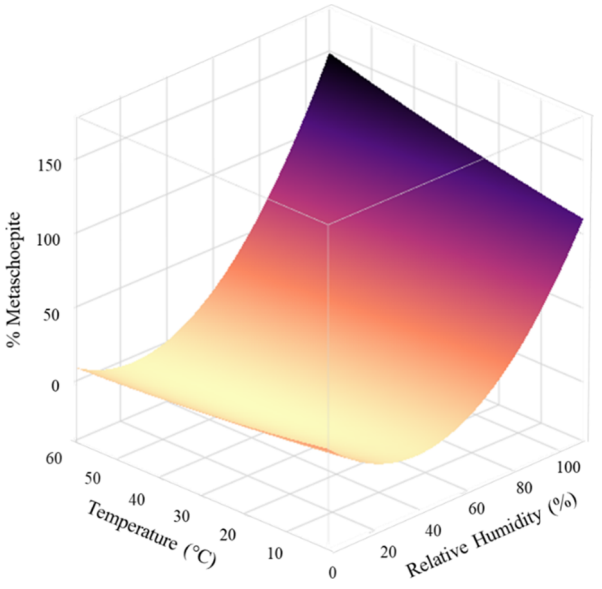

Figure 7. Response surface plot illustrating the effect of RH and temperature on the increase of metaschoepite from the hydration of A-UO_3. The response was held at center point aging conditions of 14.0 d, 30.0 °C, and 55.0%.

but the curvature from the predictive modeling indicates RH has the greater effect.

Figure 6 represents % metaschoepite as a function of aging time and temperature. In this case, temperature has very little effect on hydrolysis, while the % metaschoepite decreases as aging time increases from 0 to approximately 14 days and increases thereafter. The negative hydrolysis effect is likely the result of low to mid-range temperature (<30.0 °C) and low-range RH (≤30.0%) aging conditions at low aging times, which saw little to no increase of hydrolysis products. Figure 7 illustrates similar trends, in which increasing temperature has a lesser effect on hydrolysis, while increasing RH has a highly positive effect. Again in agreement with the Rietveld refinement and HCA results, temperature and RH both have a quantifiable effect on hydrolysis, but RH had the most significant impact.

The advancement of a response surface model illustrating the hydration and key morphological attributes of A-UO_3 is a novel development in understanding temporal changes in the $UO_3{\cdot}xH_2O$ system. This work ultimately provides valuable insights into the storage history of U-oxides, as it may be probable to utilize the speciation of A-UO_3 and its hydrolysis products to determine aging conditions such as time, temperature, and RH by a similar, inverse analysis.

CONCLUSIONS

In this study, A-UO_3 was synthesized via the uranyl peroxide synthetic route and aged under varying times, temperatures, and relative humidities. p-XRD complemented by Rietveld refinement determined the sample composition following each aging condition and illustrated each of the three aging factors play a role in A-UO_3 sample hydrolysis. SEM in conjunction with quantitative morphological analysis via MAMA and agglomerative HCA agreed with the p-XRD results and indicated longer aging times, temperatures, and relative humidities correspond to an increase in particle size. Further predictive profiling via the response surface model proved RH had the most significant impact in increasing particle morphology, corresponding to the increase of crystalline schoepite phases. This work is an important advancement to the complexity of the $UO_3{\cdot}xH_2O$ system and the U-oxide morphological data set, ultimately providing novel insight to the characterization of nuclear material provenance. While this study was highly focused on nuclear forensics, further understanding of U-oxide oxidation and hydration additionally benefits knowledgeability of the nuclear fuel cycle and uranium mobility.

ASSOCIATED CONTENT

Supporting Information

The Supporting Information is available free of charge at https://pubs.acs.org/doi/10.1021/acsomega.1c00435.

Achieved aging conditions, *R* values from Rietveld refinement analysis, discernible MAMA attributes for each aging condition and corresponding Tukey−Kramer analyses, graphical form of the DOE, physical aging setup, normalized p-XRD data, Rietveld refinement patterns, SEM imagery, segmented MAMA imagery, PCA for HCA, HCA heatmaps, and prediction profiler from the response surface methodology (PDF)

AUTHOR INFORMATION

Corresponding Author

Luther W. McDonald, IV − *Department of Civil and Environmental Engineering, Nuclear Engineering Program, University of Utah, Salt Lake City, Utah 84112, United States;* orcid.org/0000-0001-6735-5410; Phone: 1-801-581-7768; Email: luther.mcdonald@utah.edu

Authors

Alexa B. Hanson − *Department of Civil and Environmental Engineering, Nuclear Engineering Program, University of Utah, Salt Lake City, Utah 84112, United States*

https://dx.doi.org/10.1021/acsomega.1c00435
ACS Omega 2021, 6, 8605−8615

Ian J. Schwerdt − *Department of Civil and Environmental Engineering, Nuclear Engineering Program, University of Utah, Salt Lake City, Utah 84112, United States*
Cody A. Nizinski − *Department of Civil and Environmental Engineering, Nuclear Engineering Program, University of Utah, Salt Lake City, Utah 84112, United States*
Rachel Nicholls Lee − *Department of Civil and Environmental Engineering, Nuclear Engineering Program, University of Utah, Salt Lake City, Utah 84112, United States*
Nicholas J. Mecham − *Department of Civil and Environmental Engineering, Nuclear Engineering Program, University of Utah, Salt Lake City, Utah 84112, United States*
Erik C. Abbott − *Department of Civil and Environmental Engineering, Nuclear Engineering Program, University of Utah, Salt Lake City, Utah 84112, United States*
Sean Heffernan − *Department of Civil and Environmental Engineering, Nuclear Engineering Program, University of Utah, Salt Lake City, Utah 84112, United States*
Adam Olsen − *Department of Civil and Environmental Engineering, Nuclear Engineering Program, University of Utah, Salt Lake City, Utah 84112, United States*
Michael R. Klosterman − *Department of Civil and Environmental Engineering, Nuclear Engineering Program, University of Utah, Salt Lake City, Utah 84112, United States*
Sean Martinson − *Department of Civil and Environmental Engineering, Nuclear Engineering Program, University of Utah, Salt Lake City, Utah 84112, United States*
Alexandria Brenkmann − *Department of Civil and Environmental Engineering, Nuclear Engineering Program, University of Utah, Salt Lake City, Utah 84112, United States*

Complete contact information is available at: https://pubs.acs.org/10.1021/acsomega.1c00435

Author Contributions

The manuscript was written through contributions of all the authors. All the authors have given approval to the final version of the manuscript.

Notes

The authors declare no competing financial interest.

■ ACKNOWLEDGMENTS

The synthesis and aging of A-UO_3 samples and their subsequent characterization by p-XRD and SEM was supported by the U.S. Department of Homeland Security, Domestic Nuclear Detection Office, under grant award no. 2015-DN-077-ARI092. The same DHS grant, along with the Defense Threat Reduction Agency, under grant award no. HDTRA1-16-1-0026 supported the quantitative analysis via MAMA. The views and conclusions contained in this document are those of the authors and should not be interpreted as necessarily representing the official policies, either expressed or implied, of the U.S. Department of Homeland Security or Defense Threat Reduction Agency. This work made use of the University of Utah Shared facilities of the Surface Analysis and Nanoscale Imaging Group sponsored by the College of Engineering, Health Sciences Center, Office of the Vice President for Research, and the Utah Science Technology and Research (USTAR) Initiative of the State of Utah.

■ REFERENCES

(1) Sweet, L. E.; Henager, C. J.; Hu, S.; Johnson, T.; Meier, D.; Peper, S.; Schwantes, J. Investigation of Uranium Polymorphs; **2011**. DOI: 10.13140/RG.2.1.3073.0004.
(2) Hoekstra, H. R.; Siegel, S. The Uranium-Oxygen rSystem: U_3O_8-UO_3. *J. Inorg. Nucl. Chem.* **1961**, *18*, 154−165.
(3) Hoekstra, H. R.; Siegel, S. The Uranium Trioxide-Water System. *J. Inorg. Nucl. Chem.* **1973**, *35*, 761−779.
(4) Greaves, C.; Fender, B. E. F. The Structure of α-UO_3 by Neutron and Electron Diffraction. *Acta Cryst.* **1972**, *28*, 3609−3614.
(5) Debets, P. C. The Structure of β-UO_3. *Acta Cryst.* **1966**, *21*, 589−593.
(6) Kim, B. H.; Lee, Y. B.; Prelas, M. A.; Ghosh, T. K. Thermal and X-Ray Diffraction Analysis Studies during the Decomposition of Ammonium Uranyl Nitrate. *J. Radioanal. Nucl. Chem.* **2012**, *292*, 1075−1083.
(7) Engmann, R.; de Wolff, P. M. The Crystal Structure of γ-UO_3. *Acta Cryst.* **1963**, *16*, 993−996.
(8) Wheeler, V. J.; Dell, R. M.; Wait, E. Uranium Trioxide and the UO_3 Hydrates. *J. Inorg. Nucl. Chem.* **1964**, *26*, 1829−1845.
(9) Christ, C. L.; Clark, J. R. Crystal Chemical Studies of Some Uranyl Oxide Hydrates. *Am. Mineral.* **1960**, *45*, 1026−1061.
(10) Evans, H. T. Uranyl Ion Coordination. *Science* **1963**, *141*, 154−158.
(11) Miller, M. L.; Finch, R. J.; Burns, P. C.; Ewing, R. C. Description and Classification of Uranium Oxide Hydrate Sheet Anion Topologies. *J. Mater. Res.* **1996**, *11*, 3048−3056.
(12) Burns, P. C.; Miller, M. L.; Ewing, R. C. U^{6+} Minerals and Inorganic Phases; a Comparison and Hierarchy of Crystal Structures. *Can. Mineral.* **1996**, *34*, 845−880.
(13) Weck, P. F.; Kim, E. Layered Uranium(vi) Hydroxides: Structural and Thermodynamic Properties of Dehydrated Schoepite α-$UO_2(OH)_2$. *Dalton Trans.* **2014**, *43*, 17191−17199.
(14) Hawthorne, F. C.; Finch, R. J.; Ewing, R. C. Structural Relations among Schoepite, Metaschoepite and "Dehydrated Schoepite.". *Can. Mineral.* **1998**, *36*, 831−845.
(15) Sweet, L. E.; Blake, T. A.; Henager, C. H.; Hu, S.; Johnson, T. J.; Meier, D. E.; Peper, S. M.; Schwantes, J. M. Investigation of the Polymorphs and Hydrolysis of Uranium Trioxide. *J. Radioanal. Nucl. Chem.* **2013**, *296*, 105−110.
(16) Tamasi, A. L.; Cash, L. J.; Mullen, W. T.; Pugmire, A. L.; Ross, A. R.; Ruggiero, C. E.; Scott, B. L.; Wagner, G. L.; Walensky, J. R.; Wilkerson, M. P. Morphology of U_3O_8 Materials Following Storage under Controlled Conditions of Temperature and Relative Humidity. *J. Radioanal. Nucl. Chem.* **2017**, *311*, 35−42.
(17) Guo, X.; Wu, D.; Ushakov, S. V.; Shvareva, T.; Xu, H.; Navrotsky, A. Energetics of Hydration on Uranium Oxide and Peroxide Surfaces. *J. Mater. Res.* **2019**, *34*, 3319−3325.
(18) Tamasi, A. L.; Boland, K. S.; Czerwinski, K.; Ellis, J. K.; Kozimor, S. A.; Martin, R. L.; Pugmire, A. L.; Reilly, D.; Scott, B. L.; Sutton, A. D.; Wagner, G. L.; Walensky, J. R.; Wilkerson, M. P. Oxidation and Hydration of U_3O_8 Materials Following Controlled Exposure to Temperature and Humidity. *Anal. Chem.* **2015**, *87*, 4210−4217.
(19) Schwerdt, I. J.; Brenkmann, A.; Martinson, S.; Albrecht, B. D.; Heffernan, S.; Klosterman, M. R.; Kirkham, T.; Tasdizen, T.; McDonald IV, L. W. Nuclear Proliferomics: A New Field of Study to Identify Signatures of Nuclear Materials as Demonstrated on Alpha-UO_3. *Talanta* **2018**, *186*, 433−444.
(20) Schwerdt, I. J.; Hawkins, C. G.; Taylor, B.; Brenkmann, A.; Martinson, S.; McDonald IV, L. W. Uranium Oxide Synthetic Pathway Discernment through Thermal Decomposition and Morphological Analysis. *Radiochim. Acta* **2018**, *107*, 193−205.
(21) Abbott, E. C.; Brenkmann, A.; Galbraith, C.; Ong, J.; Schwerdt, I. J.; Albrecht, B. D.; Tasdizen, T.; McDonald IV, L. W. Dependence

of UO_2 Surface Morphology on Processing History within a Single Synthetic Route. *Radiochim. Acta* **2019**, *107*, 1121−1131.
(22) Schwerdt, I. J.; Olsen, A.; Lusk, R.; Heffernan, S.; Klosterman, M.; Collins, B.; Martinson, S.; Kirkham, T.; McDonald, L. W. Nuclear Forensics Investigation of Morphological Signatures in the Thermal Decomposition of Uranyl Peroxide. *Talanta* **2018**, *176*, 284−292.
(23) Olsen, A. M.; Schwerdt, I. J.; Richards, B.; McDonald, L. W. Quantification of High Temperature Oxidation of U_3O_8 and UO_2. *J. Nucl. Mater.* **2018**, *508*, 574−582.
(24) Heffernan, S. T.; Ly, N.-C.; Mower, B. J.; Vachet, C.; Schwerdt, I. J.; Tasdizen, T.; McDonald IV, L. W. Identifying Surface Morphological Characteristics to Differentiate between Mixtures of U_3O_8 Synthesized from Ammonium Diuranate and Uranyl Peroxide. *Radiochim. Acta* **2019**, *108*, 29−36.
(25) Hanson, A. B.; Lee, R. N.; Vachet, C.; Schwerdt, I. J.; Tasdizen, T.; McDonald, L. W. Quantifying Impurity Effects on the Surface Morphology of α-U_3O_8. *Anal. Chem.* **2019**, *91*, 10081−10087.
(26) Nizinski, C. A.; Hanson, A. B.; Fullmer, B. C.; Mecham, N. J.; Tasdizen, T.; McDonald, L. W. Effects of Process History on the Surface Morphology of Uranium Ore Concentrates Extracted from Ore. *Miner. Eng.* **2020**, *156*, 106457.
(27) Hanson, B. D.; McNamara, B.; Buck, E.; Friese, J.; Jenson, E.; Krupka, K.; Arey, B. Corrosion of Commercial Spent Nuclear Fuel. 1. Formation of Studtite and Metastudtite. *Radiochim. Acta* **2005**, *93*, 159−168.
(28) Ewing, R. C. Long-Term Storage of Spent Nuclear Fuel. *Nat. Mater.* **2015**, *14*, 252−257.
(29) Lezama-Pacheco, J. S.; Cerrato, J. M.; Veeramani, H.; Alessi, D. S.; Suvorova, E.; Bernier-Latmani, R.; Giammar, D. E.; Long, P. E.; Williams, K. H.; Bargar, J. R. Long-Term in Situ Oxidation of Biogenic Uraninite in an Alluvial Aquifer: Impact of Dissolved Oxygen and Calcium. *Environ. Sci. Technol.* **2015**, *49*, 7340−7347.
(30) Bone, S. E.; Cahill, M. R.; Jones, M. E.; Fendorf, S.; Davis, J.; Williams, K. H.; Bargar, J. R. Oxidative Uranium Release from Anoxic Sediments under Diffusion-Limited Conditions. *Environ. Sci. Technol.* **2017**, *51*, 11039−11047.
(31) International Atomic Energy Agency. *Technical Report Series No. 359: Uranium Extraction Technology*, 1993: Vienna.
(32) Cordfunke, E. H. P.; Van Der Giessen, A. A. Pseudomorphic Decomposition of Uranium Peroxide into UO_3. *J. Inorg. Nucl. Chem.* **1963**, *25*, 553−555.
(33) SAS Institute Inc. *JMP 15 Design of Experiments Guide*, 2019: Cary, NC.
(34) Myers, R. H.; Montgomery, D. C.; Anderson-Cook, C. M. *Response Surface Methodology: Process and Product Optimization Using Designed Experiments*, 4th ed.; Wiley, 2016.
(35) U.S. Department of Commerce. *NIST/SEMATECH e-Handbook of Statistical Methods*, 2012.
(36) ASTM Subcommittee D22.11. *Standard Practice for Maintaining Constant Relative Humidity by Means of Aqueous Solutions, 11.07; Active Standard ASTM E104*, 2012.
(37) Reilly, D. Molecular Forensic Science Analysis of Nuclear Materials. Ph.D. Thesis, University of Nevada, 2012.
(38) Ruggiero, C. E.; Bloch, J. *J. Morphological Analysis for Material Attribution (MAMA)*, Version 2.1.; Los Alamos National Laboratory, 2016.
(39) Olsen, A. M.; Richards, B.; Schwerdt, I.; Heffernan, S.; Lusk, R.; Smith, B.; Jurrus, E.; Ruggiero, C.; McDonald, L. W. Quantifying Morphological Features of α-U_3O_8 with Image Analysis for Nuclear Forensics. *Anal. Chem.* **2017**, *89*, 3177−3183.
(40) SAS Institute Inc. *JMP Pro*, Version 15.0.0: Cary, NC.
(41) *Intellectus Statistics [Online Computer Software]*, 2019.
(42) Day, W. H. E.; Edelsbrunner, H. Efficient Algorithms for Agglomerative Hierarchical Clustering Methods. *J. Classif.* **1984**, *1*, 7−24.
(43) Murtagh, F.; Contreras, P. Algorithms for Hierarchical Clustering: An Overview. *Wiley Interdiscip. Rev. Data Min. Knowl. Discov.* **2012**, *2*, 86−97.
(44) Blashfield, R. K. Mixture Model Tests of Cluster Analysis: Accuracy of Four Agglomerative Hierarchical Methods. *Psychol. Bull.* **1976**, *83*, 377−388.
(45) Degen, T.; Sadki, M.; Bron, E.; König, U.; Nénert, G. The HighScore Suite. *Powder Diffr.* **2014**, *29*, S13−S18.
(46) Taylor, J. C.; Hurst, H. J. The Hydrogen-Atom Locations in the α and β Forms of Uranyl Hydroxide. *Acta Cryst.* **1971**, *27*, 2018−2022.
(47) Bish, D. L.; Howard, S. A. Quantitative Phase Analysis Using the Rietveld Method. *J. Appl. Crystallogr.* **1988**, *21*, 86−91.
(48) Madsen, I. C.; Scarlett, N. V. Y.; Kern, A. Description and Survey of Methodologies for the Determination of Amorphous Content via X-Ray Powder Diffraction. *Z. Kristallogr.* **2011**, *226*, 944−955.
(49) McCusker, L. B.; Von Dreele, R. B.; Cox, D. E.; Louër, D.; Scardi, P. Rietveld Refinement Guidelines. *J. Appl. Crystallogr.* **1999**, *32*, 36−50.
(50) Wilkerson, M. P.; Hernandez, S. C.; Mullen, W. T.; Nelson, A. T.; Pugmire, A. L.; Scott, B. L.; Sooby, E. S.; Tamasi, A. L.; Wagner, G. L.; Walensky, J. R. Hydration of α-UO_3 following Storage under Controlled Conditions of Temperature and Relative Humidity. *Dalton Trans.* **2020**, *49*, 10452−10462.
(51) Rodgers, C.; Dyck, B. Uranium Peroxide Precipitate Drying Temperature Relationships. *CIM J.* **2012**, *3*, 149.
(52) Inc, G. A. *Root Cause Analysis Report September 9, 2014 Incident Investigation Pressurized Drum of Yellowcake at the Honeywell Uranium Refinery*; Golder Associates Inc., 2015.
(53) Tamasi, A. L.; Cash, L. J.; Eley, C.; Porter, R. B.; Pugmire, D. L.; Ross, A. R.; Ruggiero, C. E.; Tandon, L.; Wagner, G. L.; Walensky, J. R.; Wall, A. D.; Wilkerson, M. P. A Lexicon for Consistent Description of Material Images for Nuclear Forensics. *J. Radioanal. Nucl. Chem.* **2016**, *307*, 1611−1619.
(54) Pradhan, M.; Sarkar, S.; Sinha, A. K.; Basu, M.; Pal, T. Morphology Controlled Uranium Oxide Hydroxide Hydrate for Catalysis, Luminescence and SERS Studies. *CrystEngComm* **2011**, *13*, 2878−2889.
(55) Gaschen, B. K.; Bloch, J. J.; Porter, R. B.; Ruggiero, C. E.; Oyen, D. A.; Schaffer, K. M. *LA-UR-16-25116. MAMA User Guide*, v2.0.1., 2016.
(56) Conover, W. J.; Iman, R. L. Rank Transformations as a Bridge between Parametric and Nonparametric Statistics. *Am. Statistician* **1981**, *35*, 124−129.
(57) Porter, R. B.; Ruggiero, C. E. *LA-UR-14-23625. MAMA Software Features: Qualification Verification Documentation-1*, 2014.

https://dx.doi.org/10.1021/acsomega.1c00435
ACS Omega 2021, 6, 8605−8615